Progress In Electromagnetics Research, PIER 61, 193–214, 2006

THEORETICAL FOUNDATIONS OF NEAR-FIELD-FAR-FIELD TRANSFORMATIONS WITH SPIRAL SCANNINGS

F. D'Agostino, C. Gennarelli, and G. Riccio

Dipartimento di Ingegneria dell'Informazione ed Ingegneria Elettrica
University of Salerno
Via Ponte Don Melillo, 84084 Fisciano (Salerno), Italy

C. Savarese

Dipartimento per le Tecnologie
University of Naples "Parthenope"
Via Acton 38, 80133 Naples, Italy

Abstract—In this paper, the theoretical foundations of near-field-far-field transformations with spiral scannings are revisited and a unified theory is provided. This is accomplished by introducing a sampling representation of the radiated electromagnetic field on a rotational surface from the knowledge of a nonredundant number of its samples on a spiral wrapping the surface. The obtained results are general, since they are valid for spirals wrapping on quite arbitrary rotational surfaces, and can be directly applied to the pattern reconstruction via near-field-far-field transformation techniques. Numerical tests are reported for demonstrating the accuracy of the approach and its stability with respect to random errors affecting the data.

1. INTRODUCTION

As well-known, far-field (FF) range size limitations, transportation and mounting problems can make impossible or impractical the measurement of antenna radiation patterns on a conventional FF range. In such a case, it is convenient to exploit near-field (NF) measurements to recover the FF patterns via NF-FF transformation techniques. Development and spreading of NF-FF transformations employing planar, cylindrical or spherical scanning systems are

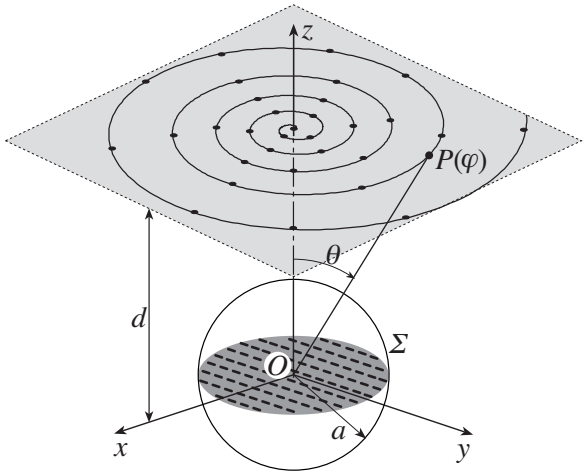

Figure 1. Planar spiral scanning.

justified from the fact that each approach has its particular advantages and limitations.

As suggested in [1], complexity and cost of the measurement set-up, as well as the time needed for data acquisition, can be reduced by means of continuous movements of the positioning systems of the probe and the antenna under test (AUT). This has induced the authors to develop innovative spiral scanning techniques. In particular, a planar spiral arrangement of samples has been considered in [2] (see Fig. 1), an innovative cylindrical NF-FF transformation with helicoidal scanning (Fig. 2) has been developed in [3, 4] and an efficient NF-FF transformation with spherical spiral scanning (Fig. 3) has been proposed in [5]. In all the cases, a nonredundant sampling representation of the voltage data acquired by the measurement probe on the considered curve (spiral or helix) has been developed by applying the theoretical results relevant to the representations of electromagnetic (EM) fields [6] and assuming the AUT enclosed in a ball of radius a. In addition, the choice of the elevation step of the curve equal to the sample spacing required to interpolate the data along the corresponding meridian curve (radial line, generatrix, meridian) has allowed one to obtain a two-dimensional optimal sampling interpolation (OSI) formula for reconstructing the voltage at any point on the surface. In such a way, the NF data needed by the NF-FF transformations employing the corresponding conventional scans [7] can be determined.

The aim of this paper is to unify the theoretical analysis of such

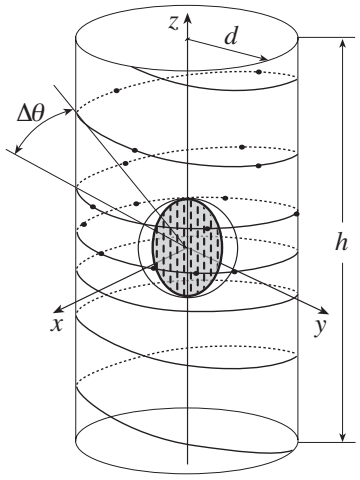

Figure 2. Helicoidal scanning.

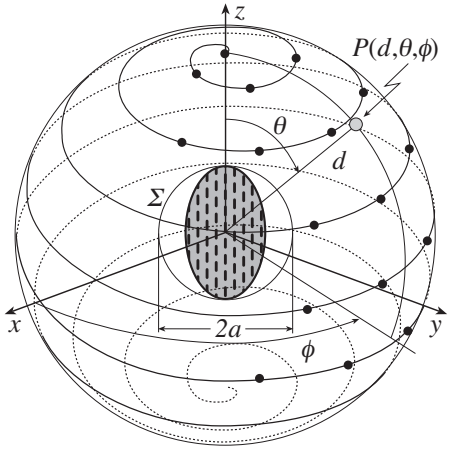

Figure 3. Spherical spiral scanning.

spiral scans and to apply the results to the FF reconstruction via NF-FF transformation techniques. This is achieved by proving that the radiated EM field and, as a consequence, the voltage acquired by a nondirective probe can be reconstructed on a quite arbitrary rotational surface from the knowledge of a nonredundant number of their samples lying on a proper spiral wrapping the surface. The only required condition is that such a surface is obtained by rotating a meridian curve always external to the cone of vertex at the observation point

and tangent to the AUT ball. This proof is achieved by starting from the results in [6] and revisiting the approach for obtaining the optimal phase function to extract from the field expression and the parameter to be used for describing the scanning curve.

It must be stressed that the field (voltage) can be reconstructed by using always the same interpolation scheme, even if the spiral lies on surfaces very different from the geometrical viewpoint. In light of the above discussion, the analysis of spiral scannings results to be unified.

2. NONREDUNDANT SAMPLING REPRESENTATION OF THE EM FIELD

The goal of this Section is to develop a sampling representation of the radiated EM field on a rotational surface from the knowledge of a nonredundant number of its samples on a spiral wrapping the surface. Such an arbitrary surface is obtained by rotating a meridian curve (a radial line allows one to construct a plane) always external to the cone tangent to the AUT ball and having the vertex at the observation point. The spiral can be viewed as intersection of the surface with the line from the origin to the point which moves on a spiral wrapping, with constant step in θ, a sphere of unit radius. The first step to achieve the proposed target is represented by the development of a nonredundant sampling representation of the field on the spiral, based on the theoretical results in [6]. Once this step is achieved, the required two-dimensional interpolation formula can be obtained by choosing the angular step of the spiral coincident with the sample spacing needed to interpolate the field along the meridian curve.

According to the theoretical results in [6], if the AUT is enclosed in a sphere with radius a and the spiral is described by an analytical parameterization $\underline{r} = \underline{r}(\xi)$, it is possible to consider the "reduced electric field"

$$\underline{F}(\xi) = \underline{E}(\xi)e^{j\gamma(\xi)} \tag{1}$$

where $\gamma(\xi)$ is a phase function to be determined. The bandlimitation error, occurring when $\underline{F}$ is approximated by a spatially bandlimited function, becomes negligible as the bandwidth exceeds the critical value

$$W_\xi = \max_\xi [w(\xi)] = \max_\xi \left[\max_{\underline{r}'} \left| \frac{d\gamma(\xi)}{\mathrm{d}\xi} - \beta \frac{\partial R(\xi, \underline{r}')}{\partial \xi} \right| \right] \tag{2}$$

where $\underline{r}'$ denotes the source point, $R(\xi, \underline{r}') = |\underline{r}(\xi) - \underline{r}'|$ and β is the wavenumber. Accordingly, such an error can be controlled by choosing a bandwidth equal to $\chi' W_\xi$, $\chi' > 1$ being an excess bandwidth factor.

A nonredundant sampling representation of the EM field on the spiral can be obtained by using the following expressions for the optimal phase function and parameterization [6]:

$$\gamma(s) = \frac{\beta}{2}\int_0^s \left[\max_{\underline{r}'} \hat{R}\cdot\hat{t} + \min_{\underline{r}'} \hat{R}\cdot\hat{t}\right] \mathrm{d}s \tag{3}$$

$$\xi = \xi(s) = \frac{\beta}{2W_\xi}\int_0^s \left[\max_{\underline{r}'} \hat{R}\cdot\hat{t} - \min_{\underline{r}'} \hat{R}\cdot\hat{t}\right] \mathrm{d}s \tag{4}$$

where s is the arclength of the spiral, $\hat{t}$ is the unit vector tangent to it at the observation point P, and $\hat{R}$ is the unit vector pointing from the source point to P.

The coordinates of P are given by:

$$\begin{cases} x = r(\vartheta)\sin\vartheta\cos\varphi \\ y = r(\vartheta)\sin\vartheta\sin\varphi \\ z = r(\vartheta)\cos\vartheta \end{cases} \tag{5}$$

where $r(\vartheta)$ is specified by the meridian curve generating the rotational surface, and φ is the angular parameter describing the spiral. It is worthy to note that the spiral angle $\vartheta = k\varphi$, unlike the zenithal angle θ, can assume negative values. In fact, when the spiral describes a complete round on the surface, ϑ varies in the range $[-\pi, \pi]$. Moreover, the spiral angle φ is always continuos, whereas, according to (5), the azimuthal angle ϕ exhibits a discontinuity jump of π when the spiral crosses the poles.

The angular elevation step of the spiral must be chosen equal to the sample spacing needed to interpolate the field along the meridian curve. Then, the parameter k is such that the angular step, determined by the consecutive intersections $P(\varphi)$ and $P(\varphi + 2\pi)$ of the spiral with the meridian curve, is $\Delta\theta = 2\pi/(2M+1)$, with $M = \mathrm{Int}[\chi M'] + 1$ and $M' = \mathrm{Int}[\chi'\beta a] + 1$. Accordingly, being $\Delta\theta = 2\pi k$, it follows that $k = 1/(2M+1)$. The function $\mathrm{Int}[x]$ gives the integer part of x and $\chi > 1$ is an oversampling factor.

Note that when the surface is a plane at distance d (planar spiral) then $r(\vartheta) = d/\cos\vartheta$, if such a surface is a cylinder of radius d (helix) then $r(\vartheta) = d/\sin\vartheta$, whereas $r(\vartheta) = d$ when a spiral wrapping a sphere of radius d is considered.

Practically, it can be convenient to impose the passage of the spiral through a given point P_0 of the meridian curve at $\phi = 0$. In such a

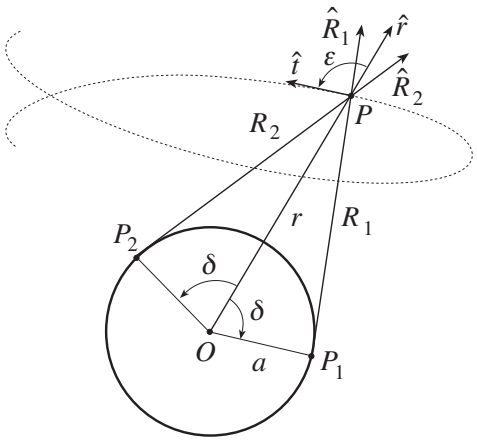

Figure 4. Geometry in the plane $\hat{t}$, $\hat{r}$.

case the coordinates of P become:

$$\begin{cases} x = r(\vartheta)\sin\vartheta\cos(\varphi-\varphi_i) \\ y = r(\vartheta)\sin\vartheta\sin(\varphi-\varphi_i) \\ z = r(\vartheta)\cos\vartheta \end{cases} \tag{6}$$

φ_i being the value of φ at P_0.

It can be verified that the extreme values of $\hat{R}\cdot\hat{t}$ in (3) and (4) are determined by considering the intersection of the plane defined by $\hat{t}$ and the unit vector $\hat{r}$ (pointing from the origin to P) with the cone with the vertex at P and the generatrices coincident with the tangents to the AUT ball. Denoting by $\hat{R}_{1,2}$ the related unit vectors and by ε the angle between $\hat{r}$ and $\hat{t}$ (Fig. 4), it results:

$$\left(\hat{R}_1+\hat{R}_2\right)/2 = \hat{r}\sin\delta = \hat{r}\sqrt{1-a^2/r^2} \tag{7}$$

$$\left(\hat{R}_1-\hat{R}_2\right)\cdot\hat{t}/2 = \cos\delta\sin\varepsilon = (a/r)\sin\varepsilon \tag{8}$$

By substituting (7) in (3), and taking into account that $\mathrm{d}r = \hat{r}\cdot\hat{t}\,\mathrm{d}s$, we get:

$$\gamma = \beta\int_0^r \sqrt{1-a^2/r^2}\,\mathrm{d}r = \beta\sqrt{r^2-a^2} - \beta a\cos^{-1}\left(\frac{a}{r}\right) \tag{9}$$

On the other hand,

$$\mathrm{d}s = \sqrt{r^2\sin^2\vartheta + k^2r^2 + k^2\dot{r}^2}\,\mathrm{d}\varphi \tag{10}$$

being $\dot{r} = \mathrm{d}r/\mathrm{d}\vartheta$. Moreover,

$$\sin\varepsilon = \sqrt{1-(\hat{r}\cdot\hat{t})^2} \tag{11}$$

wherein

$$\begin{aligned}\hat{r}\cdot\hat{t} &= \frac{\mathrm{d}r}{\mathrm{d}s} = \frac{\mathrm{d}r}{\mathrm{d}\varphi}\frac{\mathrm{d}\varphi}{\mathrm{d}s} = \left[\frac{\mathrm{d}r}{\mathrm{d}\vartheta}\frac{\mathrm{d}\vartheta}{\mathrm{d}\varphi}\right]\frac{\mathrm{d}\varphi}{\mathrm{d}s} \\ &= k\dot{r}\frac{\mathrm{d}\varphi}{\mathrm{d}s} = \frac{k\dot{r}}{\sqrt{r^2\sin^2\vartheta + k^2r^2 + k^2\dot{r}^2}}\end{aligned} \tag{12}$$

By taking into account (11) and substituting relations (8) and (10) in (4), it results:

$$\xi = \frac{\beta a}{W_\xi}\int_0^\varphi \sqrt{k^2+\sin^2 k\varphi'}\,\mathrm{d}\varphi' \tag{13}$$

As can be seen, the optimal parameter ξ is proportional to the curvilinear abscissa along the spiral wrapping the sphere of unit radius. Since such a spiral is a closed curve, it is convenient to choose the bandwidth W_ξ such that ξ covers a 2π range when the whole curve on the sphere is described. As a consequence,

$$W_\xi = \frac{\beta a}{\pi}\int_0^{(2M+1)\pi} \sqrt{k^2+\sin^2 k\varphi'}\,\mathrm{d}\varphi' \tag{14}$$

According to these results, the field at any point of the spiral can be reconstructed [6] by means of the following OSI formula of central type:

$$\underline{F}(\xi) = \sum_{n=n_0-q+1}^{n_0+q} \underline{F}(\xi_n)\Omega_{N''}(\xi-\xi_n)D_N(\xi-\xi_n) \tag{15}$$

where $n_0 = \mathrm{Int}[(\xi-\xi(\varphi_i))/\Delta\xi]$ is the index of the sample nearest (on the left) to the output point, $2q$ is the number of retained samples and

$$\xi_n = \xi(\varphi_i) + n\Delta\xi = \xi(\varphi_i) + 2\pi n/(2N+1) \tag{16}$$

with $N = \mathrm{Int}[\chi N'] + 1$ and $N' = \mathrm{Int}[\chi' W_\xi] + 1$. Moreover,

$$D_N(\xi) = \frac{\sin[(2N+1)\xi/2]}{(2N+1)\sin(\xi/2)} \tag{17}$$

$$\Omega_{N''}(\xi) = \frac{T_{N''}\left[2(\cos(\xi/2)/\cos(\xi_0/2))^2-1\right]}{T_{N''}\left[2/\cos^2(\xi_0/2)-1\right]} \tag{18}$$

are the Dirichlet and Tschebyscheff Sampling functions, respectively, wherein $N'' = N - N'$ is the Tschebyscheff polynomial degree and $\xi_0 = q\Delta\xi$.

It is worthy to note that, when interpolating the field in the neighbourhood of the poles ($\theta = 0$ and $\theta = \pi$), it is necessary to increase the excess bandwidth factor χ' in order to avoid a significant growth of the bandlimitation error. This is mainly due to the fact that small variations of ξ correspond to very large changes of φ in these zones.

Expansion (15) can be properly employed to evaluate the field at any point P on the considered surface. As a matter of fact, it allows the evaluation of the "intermediate" samples, namely the field values at the intersection points of the spiral with the meridian curve passing through P. Once these samples have been determined, because of the particular choice of $\Delta\theta$, the field can be reconstructed via the OSI expansion:

$$\underline{F}(\theta,\phi) = \sum_{m=m_0-p+1}^{m_0+p} \underline{F}(\theta_m) D_M(\theta-\theta_m)\Omega_{M''}(\theta-\theta_m) \qquad (19)$$

where

$$\theta_m = \theta_m(\phi) = \theta(\varphi_i) + k\phi + m\Delta\theta = \theta_0 + m\Delta\theta \qquad (20)$$

$\underline{F}(\theta_m)$ are the intermediate samples, $m_0 = \mathrm{Int}[(\theta-\theta_0)/\Delta\theta]$, $M'' = M - M'$ and the other symbols have the same meaning as in (15).

Since the voltage measured by a nondirective probe has the same effective spatial bandwidth of the field [8], the above OSI expansions can be used also to interpolate the "reduced voltage" $\tilde{V}(\xi) = V(\xi)e^{j\gamma(\xi)}$.

3. THE HELICOIDAL SCANNING CASE

The algorithm described in the previous Section can be applied to efficiently reconstruct the NF data, needed for the classical probe compensated NF-FF transformation [9], from the voltage samples acquired on a helix wrapping a cylinder. It must be stressed that, unlike the approach in [4], the helix originates now from a given point at the top of the cylinder, thus simplifying the realization of the scanning from the practical viewpoint. Accordingly, the parametric equations of the helix, when imposing the passage through such a point on the

generatrix at $\phi = 0$ and taking into account that $r(\vartheta) = d/\sin\vartheta$, are:

$$\begin{cases} x = d\cos(\varphi - \varphi_i) \\ y = d\sin(\varphi - \varphi_i) \\ z = d\cot\vartheta \end{cases} \tag{21}$$

As shown in [9], the modal coefficients a_υ and b_υ of the cylindrical wave expansion of the field radiated by the AUT are related to: a) the two-dimensional Fourier transforms I_υ and I'_υ of the output voltages V and V' of the probe for two independent sets of measurements (the probe is rotated 90° about its longitudinal axis in the second set); b) the modal coefficients of the cylindrical wave expansion of the field radiated by the probe and the rotated probe, when used as transmitting antennas. The key relations are summarized in the following for reader's convenience:

$$\begin{aligned} a_\upsilon(\eta) \;=\; & \frac{\beta^2}{\Lambda^2\Delta_\upsilon(\eta)}\left[I_\upsilon(\eta)\sum_{m=-\infty}^{\infty} d'_m(-\eta)H^{(2)}_{\upsilon+m}(\Lambda d)\right. \\ & \left. - I'_\upsilon(\eta)\sum_{m=-\infty}^{\infty} d_m(-\eta)H^{(2)}_{\upsilon+m}(\Lambda d)\right] \end{aligned} \tag{22}$$

$$\begin{aligned} b_\upsilon(\eta) \;=\; & \frac{\beta^2}{\Lambda^2\Delta_\upsilon(\eta)}\left[I'_\upsilon(\eta)\sum_{m=-\infty}^{\infty} c_m(-\eta)H^{(2)}_{\upsilon+m}(\Lambda d)\right. \\ & \left. - I_\upsilon(\eta)\sum_{m=-\infty}^{\infty} c'_m(-\eta)H^{(2)}_{\upsilon+m}(\Lambda d)\right] \end{aligned} \tag{23}$$

where $\Lambda = \sqrt{\beta^2 - \eta^2}$, $H^{(2)}_\upsilon(\cdot)$ is the Hankel function of second kind and order υ,

$$\begin{aligned} I_\upsilon(\eta) \;&=\; \int_{-\infty}^{\infty}\int_{-\pi}^{\pi} V(\phi, z)e^{-j\upsilon\phi}e^{j\eta z}\,\mathrm{d}\phi\,\mathrm{d}z; \\ I'_\upsilon(\eta) \;&=\; \int_{-\infty}^{\infty}\int_{-\pi}^{\pi} V'(\phi, z)e^{-j\upsilon\phi}e^{j\eta z}\,\mathrm{d}\phi\,\mathrm{d}z \end{aligned} \tag{24}$$

and

$$\begin{aligned} \Delta_\upsilon(\eta) \;=\; & \sum_{m=-\infty}^{\infty} c_m(-\eta)H^{(2)}_{\upsilon+m}(\Lambda d)\sum_{m=-\infty}^{\infty} d'_m(-\eta)H^{(2)}_{\upsilon+m}(\Lambda d) \\ & - \sum_{m=-\infty}^{\infty} c'_m(-\eta)H^{(2)}_{\upsilon+m}(\Lambda d)\sum_{m=-\infty}^{\infty} d_m(-\eta)H^{(2)}_{\upsilon+m}(\Lambda d) \end{aligned} \tag{25}$$

The modal coefficients associated to the probe (c_m, d_m) and the rotated probe (c'_m, d'_m) can be determined from the measured amplitude and phase of the field radiated by them in the FF region.

In the classical approach, the FFT is employed to evaluate efficiently the modal coefficients, and the sample spacings of the NF data [9] are $\Delta z \leq \lambda/2$ and $\Delta\phi \leq \lambda/(2a')$, a' being the radius of the smallest cylinder enclosing the AUT and λ the wavelength.

Once the modal coefficients are determined, the FF components of the electric field in the spherical coordinate system (R, Θ, Φ) can be evaluated by:

$$E_\Theta = -j2\beta\frac{e^{-j\beta R}}{R}\sin\Theta\sum_{v=-\infty}^{\infty} j^v b_v(\beta\cos\Theta)e^{jv\Phi} \tag{26}$$

$$E_\Phi = -2\beta\frac{e^{-j\beta R}}{R}\sin\Theta\sum_{v=-\infty}^{\infty} j^v a_v(\beta\cos\Theta)e^{jv\Phi} \tag{27}$$

It is useful to note that the summations in the above equations can be efficiently performed via the FFT algorithm.

Some numerical tests assessing the effectiveness of the technique are reported in the following. The simulations refer to a uniform planar circular array (see Fig. 2) symmetric with respect to the plane $z = 0$ and having radius $a = 16\lambda$. Its elements are $\lambda/2$ spaced elementary Huygens sources polarized along the z axis. An open-ended WR-90 rectangular waveguide, operating at the frequency of 10 GHz, is chosen as probe. The NF data are collected on a helix wrapping the cylinder with radius $d = 25\lambda$ and height $h = 220\lambda$. Figures 5 and 6 show the reconstruction of the amplitude and phase of the output voltage V on the cylinder generatrix at $\phi = 90°$. As can be seen, the reconstruction is everywhere very accurate. The accuracy of the NF interpolation process is also confirmed by the values of the maximum and mean-square errors (normalized to the voltage maximum value on the cylinder) reported in Figs. 7 and 8, respectively. They have been obtained by comparing the interpolated values of V with those directly evaluated on a close grid in the central zone of the cylinder, so that the existence of the guard samples is assured. As expected, the errors decrease up to very low values on increasing the oversampling factor and/or the number of the retained samples. The stability of the algorithm has been investigated by adding random errors to the exact samples. These errors simulate a background noise, bounded to Δa (dB) in amplitude and with arbitrary phase, and an uncertainty on the data of $\pm\Delta a_r$ (dB) in amplitude and $\pm\Delta\alpha$ (degrees) in phase. As shown in Fig. 9, the algorithm is stable.

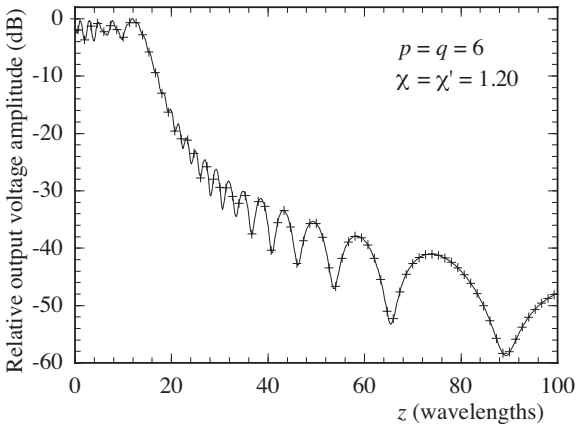

Figure 5. Helicoidal scanning. Amplitude of V on the generatrix at $\phi = 90°$. Solid line: exact. Crosses: interpolated.

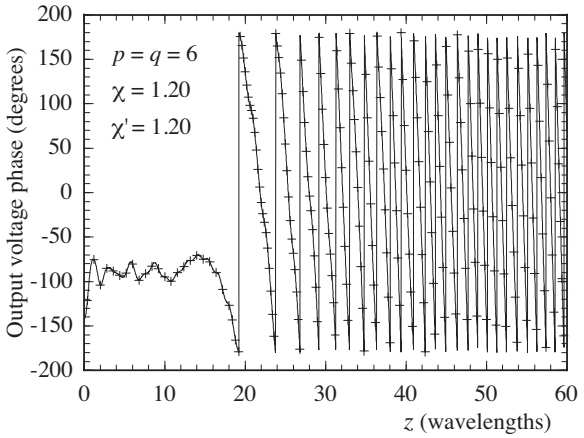

Figure 6. Helicoidal scanning. Phase of V on the generatrix at $\phi = 90°$. Solid line: exact. Crosses: interpolated.

The reconstructions of the antenna FF pattern in the principal planes are reported in Figs. 10 and 11. As can be seen, the exact and recovered fields are practically indistinguishable, thus assessing the effectiveness of the proposed probe compensated NF-FF transformation technique.

It is worthy to note that the number of employed samples (guard samples included) for reconstructing the NF data on the considered cylinder is 26 552, less than half of that (59 265) needed by the

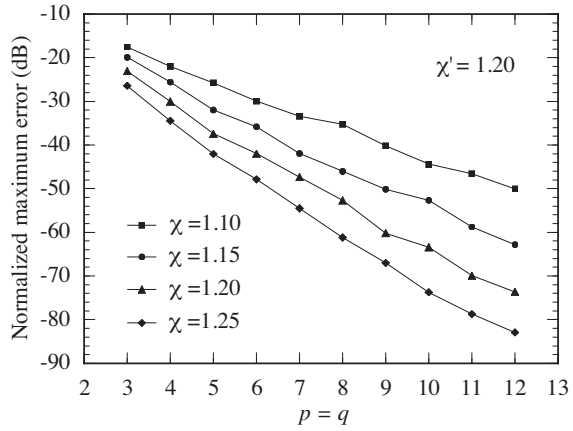

Figure 7. Helicoidal scanning. Maximum reconstruction error of V.

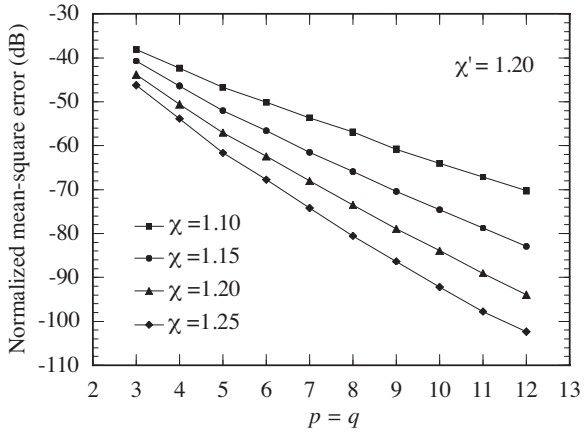

Figure 8. Helicoidal scanning. Mean-square reconstruction error of V.

approach in [3] and significantly less than that (112 640) required by the approach in [9].

4. THE PLANAR SPIRAL CASE

A fast and accurate NF-FF transformation technique with planar spiral scanning, which compensates for the effects of the measurement probe, is briefly described in this Section. For a planar spiral $r(\vartheta) = d/\cos\vartheta$,

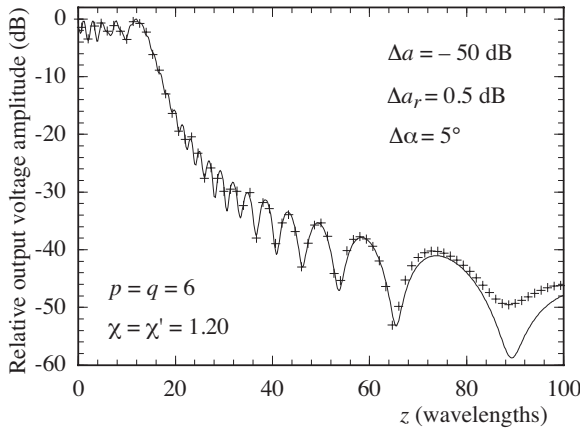

Figure 9. Helicoidal scanning. Amplitude of V on the generatrix at $\phi = 90°$. Solid line: exact. Crosses: reconstructed from error affected data.

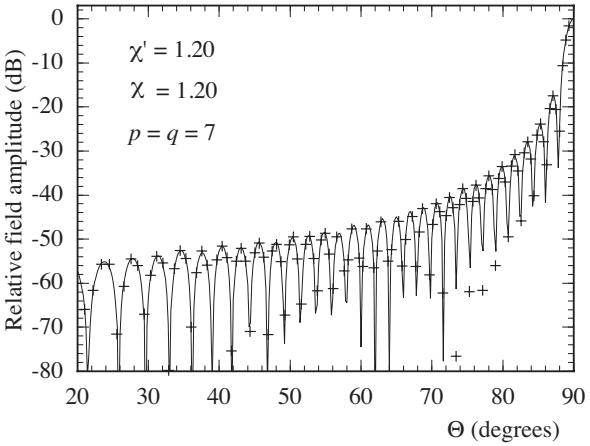

Figure 10. Helicoidal scanning. E-plane pattern. Solid line: exact. Crosses: reconstructed from probe compensated NF measurements.

so that the coordinates of a point lying on it are given by:

$$\begin{cases} x = d\tan\vartheta\cos\varphi = \rho\cos\varphi \\ y = d\tan\vartheta\sin\varphi = \rho\sin\varphi \\ z = d \end{cases} \tag{28}$$

Also in such a case, the algorithm proposed in Section 2 can

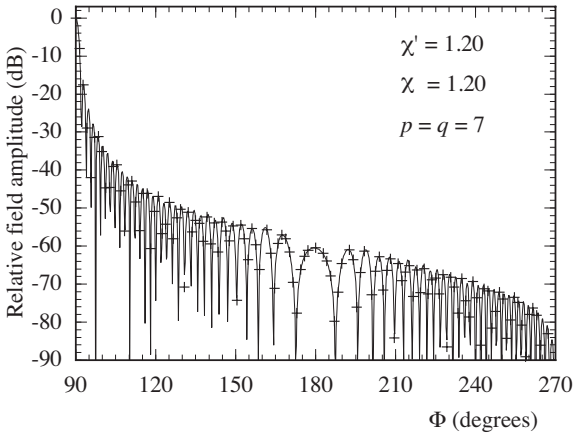

Figure 11. Helicoidal scanning. H-plane pattern. Solid line: exact. Crosses: reconstructed from probe compensated NF measurements.

be properly applied to efficiently reconstruct the NF data, needed by the probe compensated NF-FF transformation employing the corresponding conventional scan, from the knowledge of the voltage samples acquired on the spiral.

The basic theory of probe compensated NF-FF transformation with plane-rectangular scanning as proposed by Paris et alii in [10] is based on the application of the Lorentz reciprocity theorem. The key relations in the here used reference system are:

$$E_\Theta(\Theta,\Phi) = \left(I_H E'_{\Phi_V}(\Theta,-\Phi) - I_V E'_{\Phi_H}(\Theta,-\Phi)\right)/\Delta \tag{29}$$

$$E_\Phi(\Theta,\Phi) = \left(I_H E'_{\Theta_V}(\Theta,-\Phi) - I_V E'_{\Theta_H}(\Theta,-\Phi)\right)/\Delta \tag{30}$$

where

$$\Delta = E'_{\Theta_H}(\Theta,-\Phi)E'_{\Phi_V}(\Theta,-\Phi) - E'_{\Theta_V}(\Theta,-\Phi)E'_{\Phi_H}(\Theta,-\Phi) \tag{31}$$

$$I_{V,H} = C\cos\Theta e^{j\beta d\cos\Theta}\int_{-\infty}^{+\infty}\int_{-\infty}^{+\infty} V_{V,H}(x,y)e^{j\beta x\sin\Theta\cos\Phi}e^{j\beta y\sin\Theta\sin\Phi}\,\mathrm{d}x\,\mathrm{d}y \tag{32}$$

C being a constant. Namely, the antenna far field is related to: i) the two-dimensional Fourier transforms I_V and I_H of the output voltages V_V and V_H of the probe for two independent sets of measurements (the probe is rotated by 90° in the second set); ii) the FF components

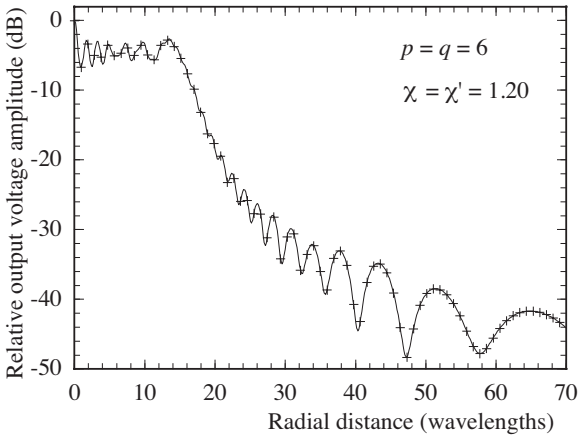

Figure 12. Planar spiral scanning. Amplitude of V_V on the radial line at $\phi = 90°$. Solid line: exact. Crosses: interpolated.

E'_{Θ_V}, E'_{Φ_V} and E'_{Θ_H}, E'_{Φ_H} radiated by the probe and the rotated probe, when used as transmitting antennas.

In order that equations (29) and (30) are valid, the probe must maintain its orientation with respect to the AUT and this requires its co-rotation with the AUT. Obviously, the positioning system is remarkably simplified when this is avoided. Probes exhibiting only a first-order azimuthal dependence in their radiated far field (such as, f.i., an open-ended circular waveguide excited by a TE_{11} mode) can be used without co-rotation, since V_V and V_H can be evaluated from the knowledge of the measured voltages V_ϕ and V_ρ, through the relations:

$$V_V = V_\phi \cos\phi - V_\rho \sin\phi; \qquad V_H = V_\phi \sin\phi + V_\rho \cos\phi \tag{33}$$

In the following we report some numerical tests, which assess the effectiveness of the technique. They refer to a uniform planar circular array (see Fig. 1) having diameter $2a = 33.6\lambda$. Its elements are elementary Huygens sources linearly polarized along the y axis and are radially and azimuthally spaced of 0.7λ. An open-ended circular waveguide with radius $a' = 0.338\lambda$ is chosen as probe. The measurement plane is 20λ away from the AUT center and the samples of the probe voltages V_ϕ and V_ρ are collected on a spiral that covers a circular zone of radius $\approx 71\lambda$, without considering the guard samples. Figure 12 shows the reconstruction of the amplitude of the output voltage V_V (the most significant one) on the radial line at $\phi = 90°$. As can be seen, there is an excellent agreement between the exact voltage and the reconstructed one. It is worthy to note that, in the

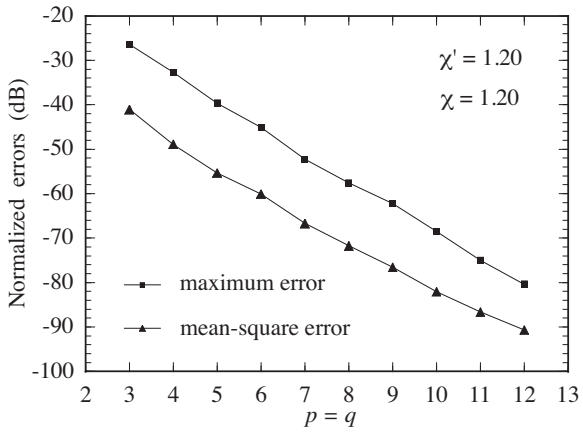

Figure 13. Planar spiral scanning. Normalized reconstruction errors of V_V.

zone of the spiral determined by the 23 "regular" samples centered on the pole, we have adopted an excess bandwidth factor such that the sample spacing is reduced by a factor 5. The accuracy of the algorithm is also confirmed by the values of the maximum and mean-square errors (normalized to the voltage maximum value on the plane) in the reconstruction of V_V. Those reported in Fig. 13 are relevant to $\chi' = \chi = 1.20$ and have been obtained by comparing the interpolated values of V_V with those directly evaluated on a close grid in the central zone of the plane, so that the existence of the guard samples is assured.

The E-plane pattern, reconstructed from the recovered plane-rectangular data lying in a $100\lambda \times 100\lambda$ square grid, is shown (crosses) in Fig. 14. The pattern reconstructed (via the uncompensated NF-FF transformation) from the exact plane-rectangular field samples lying in the same grid is reported as reference (solid line) in the same figure. As can be seen, also the FF reconstruction is very accurate, thus assessing the effectiveness of the technique.

Note that the number of samples over the spiral is 12 823, practically the same than that (13 309) needed by the plane-polar NF-FF transformation [11]. In particular, the number of "regular" samples at spacing $\Delta\xi$ is 12 735, whereas the number of "extra" samples at reduced spacing $\Delta\xi/5$ is only 88. It may be interesting to compare the number of data needed by the proposed technique also with those required by applying other planar scanning techniques. With reference to the considered example, this number is 126 665 for the plane-polar NF-FF transformation [12] and becomes 40 000 for the classical plane-

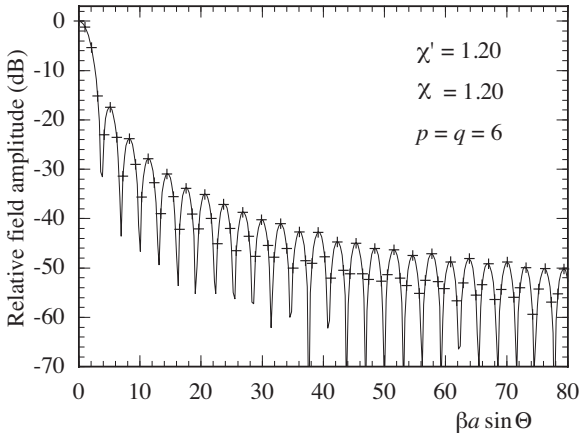

Figure 14. Planar spiral scanning. E-plane pattern. Solid line: reference. Crosses: reconstructed from probe compensated NF measurements.

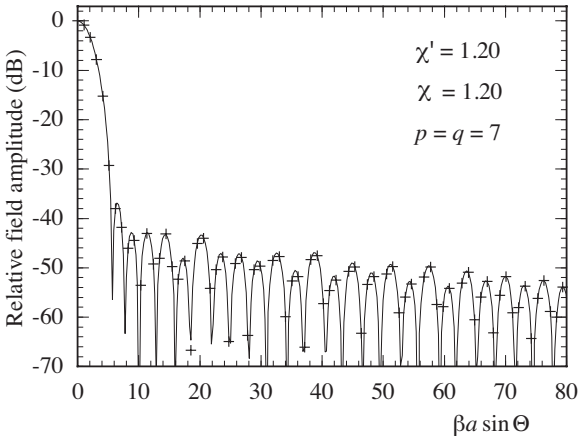

Figure 15. Planar spiral scanning. E-plane pattern of a Tschebyscheff-like planar circular array. Solid line: reference. Crosses: reconstructed from probe compensated NF measurements.

rectangular NF-FF transformation [10] at $\lambda/2$ spacings.

At last, the algorithm performance has been tested in more severe conditions by changing the excitations of the array elements in order to obtain a Tschebyscheff-like behaviour with SLR = 40 dB in the FF region. Also in this case (see Fig. 15) the reconstruction is very good.

5. THE SPHERICAL SPIRAL CASE

Also in such a case, the NF data required by one of the available probe compensated NF-FF transformations with spherical scanning can be accurately recovered from the voltage samples collected on the spiral by employing the algorithm described in Section 2. It must be stressed that, unlike the approach in [5], the spiral originates now from the pole at $\theta = 0$. Accordingly, by taking into account that $r(\vartheta) = d$, the coordinates of a point lying on the spherical spiral are:

$$\begin{cases} x = d\sin\vartheta\cos\varphi \\ y = d\sin\vartheta\sin\varphi \\ z = d\cos\vartheta \end{cases} \tag{34}$$

To make more efficient the FF reconstruction, the theoretical aspects of the classical method [13] have been re-examined in [14, 15] by taking into account the spatial bandlimitation properties of the radiated EM fields [16]. In particular, the choice of the highest spherical wave has been rigorously fixed by the bandlimitation properties and the number of data on the parallels has resulted to be decreasing towards the poles. The key relations are here reported for reader's convenience.

The tangential electric field in the FF region can be expressed via the truncated spherical wave expansion:

$$\underline{E}_t(R\to\infty,\Theta,\Phi) = \frac{e^{-j\beta R}}{R}\sum_{n=1}^{N_{\max}}\sum_{m=-n}^{n}\left[j^{n+1}b_{nm}^1\underline{\tilde{f}}_{1nm}(\Theta)+j^n b_{nm}^2\underline{\tilde{f}}_{2nm}(\Theta)\right]e^{jm\Phi} \tag{35}$$

wherein the highest spherical wave is rigorously fixed [14] by

$$N_{\max} = \mathrm{Int}[\chi'\beta a] + 1. \tag{36}$$

The expansion coefficients b_{nm}^1 and b_{nm}^2 can be evaluated from the knowledge of the voltages V and V' measured by the probe and rotated probe, respectively. The explicit expressions of the modal coefficients and vector wave functions $\underline{\tilde{f}}_{1nm}, \underline{\tilde{f}}_{2nm}$ can be found in [15].

By inverting the summation order in (35), it can be rewritten [14] as follows:

$$\underline{E}_t(R\to\infty,\Theta,\Phi) = \frac{e^{-j\beta R}}{R}\sum_{m=-M_\phi}^{M_\phi}\underline{c}_m(\Theta)e^{jm\Phi} \tag{37}$$

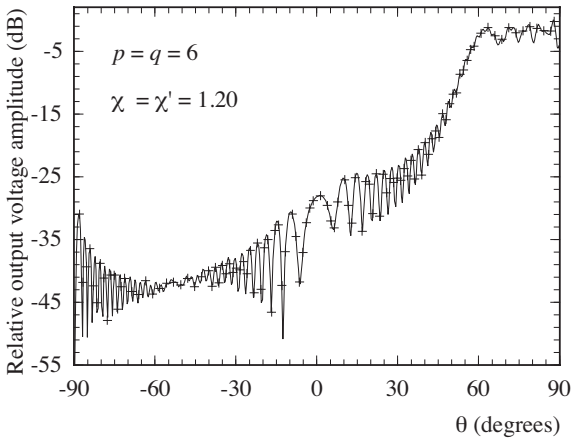

Figure 16. Spherical spiral scanning. Amplitude of V' on the meridian at $\phi = 90°$. Solid line: exact. Crosses: interpolated.

where $M_\phi = \mathrm{Int}[\chi' \beta a \sin\theta] + 1$. Relation (37) allows an efficient evaluation of the AUT far field at the considered elevation angle Θ by performing the summation via FFT.

Many numerical tests have been performed to confirm the validity of the proposed technique. The reported simulations refer to a uniform planar circular array (see Fig. 3) symmetric with respect to the plane $z = 0$ and having radius $a = 18\lambda$. Its elements, elementary Huygens sources linearly polarized along the z axis, are radially and azimuthally spaced of 0.6λ. The radius of the spherical scanning surface is 30λ. An open-ended circular waveguide, having radius $a' = 0.338\lambda$, is considered as measurement probe. Figure 16 shows the reconstruction of the amplitude of the probe voltage V' on the meridian at $\phi = 90°$. As can be seen, the reconstruction is everywhere accurate. It is useful to note that we have adopted, in the zones of the spiral determined by the 40 samples around the poles, an excess bandwidth factor such that the sample spacing is reduced exactly by a factor 9. This has allowed to reconstruct accurately the intermediate samples nearby the poles and, as a consequence, the voltage. To assess in a more quantitative way the algorithm performances, the maximum and mean-square errors (normalized to the voltage maximum value on the sphere) have been evaluated. Those reported in Fig. 17 are relevant to $\chi' = \chi = 1.20$ and have been obtained by comparing the interpolated values of V' with those directly evaluated on a close grid.

At last, the proposed sampling technique has been used to recover the data required by the probe compensated NF-FF transformation

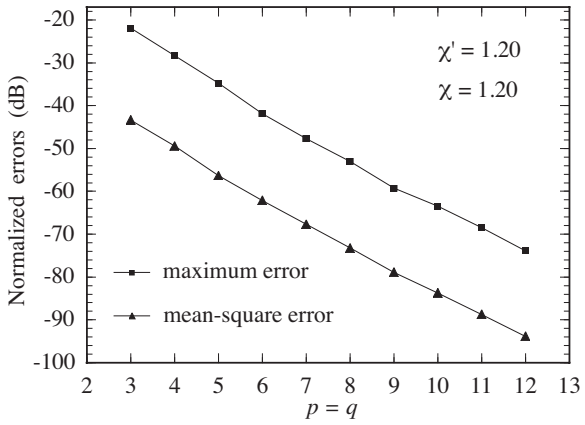

Figure 17. Spherical spiral scanning. Normalized reconstruction errors of V'.

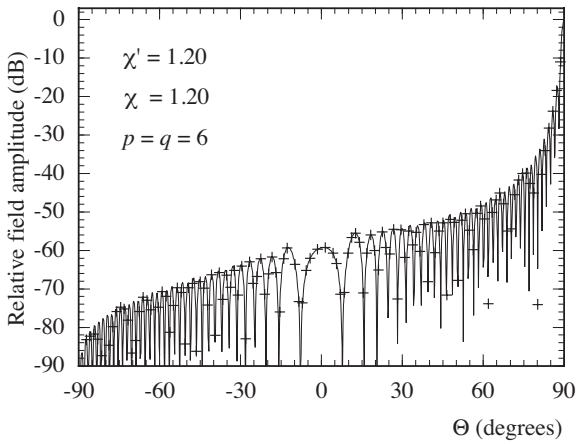

Figure 18. Spherical spiral scanning. E-plane pattern. Solid line: exact. Crosses: reconstructed from probe compensated NF measurements.

with spherical scanning as modified in [15]. A representative reconstruction example relevant to the FF Θ-component in the E plane is reported in Fig. 18.

It is useful to note that the number of samples over the spiral is 34 782, about half of that (69 282) needed by the aforementioned modified version of the NF-FF transformation and significantly less than that (130 562) required by the classical one [13]. In particular,

the number of "regular" samples at spacing $\Delta\xi$ is 34 142, whereas the number of "extra" samples at reduced spacing is 640.

6. CONCLUSIONS

A unified theory for the NF-FF transformation techniques with spiral scannings has been provided in this paper. To this end, a fast, accurate and stable sampling representation, which allows the reconstruction of the radiated EM field (probe voltage) on a quite arbitrary rotational surface from the knowledge of a nonredundant number of its samples on a spiral wrapping it, has been developed. The obtained results are general, since they are valid for spirals lying on surfaces obtained by rotating a meridian curve always external to the cone of vertex at the observation point and tangent to the AUT sphere. Some numerical tests relevant to both the cases of planar and spherical spiral scannings, as well as to the helicoidal scan, have assessed the accuracy and the stability of the approach.

ACKNOWLEDGMENT

A special acknowledgement is due to Professor Ovidio Mario Bucci whose scientific contributions have made possible the development of spiral scannings.

REFERENCES

1. Yaccarino, R. G., L. I. Williams, and Y. Rahmat-Samii, "Linear spiral sampling for the bipolar planar antenna measurement technique," *IEEE Trans. Antennas Propagat.*, Vol. AP-44, 1049–1051, 1996.
2. Bucci, O. M., F. D'Agostino, C. Gennarelli, G. Riccio, and C. Savarese, "Probe compensated FF reconstruction by NF planar spiral scanning," *IEE Proc. - Microw., Antennas Propagat.*, Vol. 149, 119–123, 2002.
3. Bucci, O. M., C. Gennarelli, G. Riccio, and C. Savarese, "Probe compensated NF-FF transformation with helicoidal scanning," *J. Electromagn. Waves Appl.*, Vol. 14, 531–549, 2000.
4. Bucci, O. M., C. Gennarelli, G. Riccio, and C. Savarese, "Nonredundant NF-FF transformation with helicoidal scanning," *J. Electromagn. Waves Appl.*, Vol. 15, 1507–1519, 2001.
5. Bucci, O. M., F. D'Agostino, C. Gennarelli, G. Riccio, and C. Savarese, "NF-FF transformation with spherical spiral

scanning," *IEEE Antennas Wireless Propagat. Lett.*, Vol. 2, 263–266, 2003.

6. Bucci, O. M., C. Gennarelli, and C. Savarese, "Representation of electromagnetic fields over arbitrary surfaces by a finite and nonredundant number of samples," *IEEE Trans. Antennas Propagat.*, Vol. 46, 351–359, 1998.
7. Gennarelli, C., G. Riccio, F. D'Agostino, and F. Ferrara, *Near-field - Far-field Transformation Techniques*, CUES, Salerno, Italy, 2004.
8. Bucci, O. M., G. D'Elia, and M. D. Migliore, "Advanced field interpolation from plane-polar samples: experimental verification," *IEEE Trans. Antennas Propagat.*, Vol. 46, 204–210, 1998.
9. Leach, W. M., Jr. and D. T. Paris, "Probe compensated NF measurements on a cylinder," *IEEE Trans. Antennas Propagat.*, Vol. AP-21, 435–445, 1973.
10. Paris, D. T., W. M. Leach, Jr., and E. B. Joy, "Basic theory of probe-compensated near-field measurements," *IEEE Trans. Antennas Propagat.*, Vol. AP-26, 373–379, 1978.
11. Bucci, O. M., C. Gennarelli, G. Riccio, and C. Savarese, "Fast and accurate far-field evaluation from a non redundant, finite number of plane-polar measurements," *Proc. of 1994 IEEE AP-S Int. Symp.*, 540–543, Seattle, USA, June 1994.
12. Gatti, M. and Y. Rahmat-Samii, "FFT applications to plane-polar near-field antenna measurements," *IEEE Trans. Antennas Propagat.*, Vol. AP-36, 781–791, 1988.
13. Hansen, J. E., *Spherical Near-field Antenna Measurements*, IEE Electromagnetic Waves Series, London, Peter Peregrinus Ltd., UK, 1998.
14. Bucci, O. M., F. D'Agostino, C. Gennarelli, G. Riccio, and C. Savarese, "Data reduction in the NF-FF transformation technique with spherical scanning," *J. Electromagn. Waves Appl.*, Vol. 15, 755–775, 2001.
15. Arena, A., F. D'Agostino, C. Gennarelli, and G. Riccio, "Probe compensated NF-FF transformation with spherical scanning from a minimum number of data," *Proc. of "G. Ronchi" Foundation*, Vol. LIX, 311–326, 2004.
16. Bucci, O. M. and G. Franceschetti, "On the spatial bandwidth of scattered fields," *IEEE Trans. Antennas Propagat.*, Vol. AP-35, 1445–1455, 1987.